⊛IDSA OXFORD

Functional and Structural Characterization of Treatment-Emergent Nirmatrelvir Resistance Mutations at Low Frequencies in the Main Protease (M^pro) Reveals a Unique Evolutionary Route for SARS-CoV-2 to Gain Resistance

Natalie M. Deschenes,[1,a] Jimena Pérez-Vargas,[2,a] Zoe Zhong,[3] Merrilee Thomas,[4] Calem Kenward,[5] Wesley A. Mosimann,[5] Liam J. Worrall,[5] Nicholas Waglechner,[6] Angel XinLiu Li,[3] Finlay Maguire,[6,7,8] Patryk Aftanas,[6] Jason R. Smith,[9] Jared Lim,[10] Robert N. Young,[9] Artem Cherkasov,[11] Lubna Farooqi,[3] Adnan Moinuddin,[3] Lina Siddiqi,[3] Imaan Malik,[3] Maxime Lefebvre,[3] Mark Paetzel,[10] Natalie C. J. Strynadka,[5] François Jean,[2,a] Allison McGeer,[3,7,a] and Robert A. Kozak[1,6,12,a]

[1]Biological Sciences Platform, Sunnybrook Research Institute, Toronto, Ontario, Canada; [2]Department of Microbiology and Immunology, Life Sciences Institute, University of British Columbia, Vancouver, British Columbia, Canada; [3]Sinai Health System, Mount Sinai Hospital, Toronto, Ontario, Canada; [4]Montana Molecular, Bozeman, Montana, USA; [5]Department of Biochemistry and Molecular Biology and Centre for Blood Research, University of British Columbia, Vancouver, British Columbia, Canada; [6]Shared Hospital Laboratory, Toronto, Ontario, Canada; [7]Faculty of Computer Science, Dalhousie University, Halifax, Nova Scotia, Canada; [8]Department of Community Health and Epidemiology, Dalhousie University, Halifax, Nova Scotia, Canada; [9]Department of Chemistry, Simon Fraser University, Burnaby, British Columbia, Canada; [10]Department of Molecular Biology and Biochemistry, Simon Fraser University, Burnaby, British Columbia, Canada; [11]Vancouver Prostate Centre, University of British Columbia, Vancouver, British Columbia, Canada; and [12]Department of Laboratory Medicine and Pathology, University of Toronto, Toronto, Ontario, Canada

Background. The main protease (M^pro) is one of the most attractive targets for antiviral drug discovery against severe acute respiratory syndrome coronavirus 2 (SARS-CoV-2). Mutations in M^pro have been linked to resistance against nirmatrelvir-ritonavir (NIR-RIT), an important therapy for SARS-CoV-2 infection. This study aimed to identify low-frequency antiviral resistance mutations in M^pro from NIR-RIT–treated patients and to analyze the enzymatic properties, inhibitor susceptibility, and structural features of new M^pro clinical variants.

Methods. We screened 1528 SARS-CoV-2–positive patients from 2 hospitals and identified 17 who remained positive after treatment. Whole-genome sequencing of nasopharyngeal specimens was conducted to identify M^pro clinical variants. The impact of these mutations on M^pro activity and inhibitor susceptibility was investigated using a fluorescent enzymatic biosensor in human cells, along with in vitro thermal stability and structure-based analyses of the M^pro mutants and M^pro-NIR complexes.

Results. The analysis identified 2 novel M^pro clinical variants: D48D/L58F/P132H (variant 1) and D48D/L67V/K90R/P132H (variant 2). Our data show that the selected clinical mutations are localized in the M^pro N-terminal domain, are far from the catalytic site, and strongly impact NIR resistance without affecting M^pro activity. Structural analysis and thermal denaturation analyses revealed that these mutations may disrupt the substrate binding site's structure and dynamics, reducing protein stability and potentially impacting substrate binding or dimerization without compromising catalytic activity.

Conclusions. Our new M^pro clinical mutations that confer complete resistance to NIR were not identified during previous cell-culture-based studies. More research is needed to explore resistance mechanisms, providing insights into strategies that mitigate resistance and protect therapeutic efficacy.

Keywords. COVID-19; SARS-CoV-2; main protease inhibitor; nirmatrelvir-ritonavir; low-frequency resistance mutations.

https://doi.org/10.1093/infdis/jiaf294

Nirmatrelvir-ritonavir (NIR-RIT) has reduced disease severity and improved clinical outcomes for individuals infected with severe acute respiratory syndrome coronavirus 2 (SARS-CoV-2) [1, 2], including significantly reducing hospitalizations in elderly and immunocompromised individuals [3, 4]. This antiviral inhibits the SARS-CoV-2 chymotrypsin-like protease (3CLpro or M^pro) [2]. M^pro is essential for cleaving viral polyproteins into functional proteins required for replication [5]. By binding the active site, NIR blocks this cleavage, disrupting viral protein production and replication [2, 6].

The M^pro protein consists of 3 domains: domain I (residues 8–101), domain II (residues 102–184), and domain III (residues 201–303) [7, 8]. The substrate binding site is located at the cleft between domains I and II. Though not directly catalytic,

domain III is crucial for dimerization, as M^{pro} is catalytically inactive as a monomer [9]. Several studies have identified NIR-RIT resistance mutations through in vitro experimentation. Among these, mutations such as L50F and E166A/V have been associated with high-level resistance, as they directly impact the enzyme's active site, reducing susceptibility to NIR-RIT [10–14]. Other common mutations, such as P132H and K90R, lie outside the active site, but still impact M^{pro} structure and dynamics, reducing inhibitor efficacy [13].

Research on these mutations in clinical samples from treated patients remains limited and while in vitro studies provide insights, viral behavior may differ in vivo [15]. Large-scale surveillance has found that resistance mutations are infrequent [16, 17]. Nevertheless, cases of resistance to antiviral therapies have been documented, particularly among immunocompromised individuals [18, 19]. Although resistance in clinical isolates is rare [20], low-frequency variants may not be captured in consensus sequences. Resistance may arise from suboptimal therapy or incomplete treatment, as seen in human immunodeficiency virus 1 (HIV-1) [21, 22] and hepatitis C virus [23, 24]. This can lead to the selection of low-frequency antiviral resistance variants, which may become dominant. Therefore, assessing the prevalence of these mutations in clinical samples is crucial.

Our study investigated the emergence of low-frequency antiviral resistance variants in patients with SARS-CoV-2 after receiving NIR-RIT. We used whole-genome sequencing to identify these variants in patients who had completed a partial or full 5-day course of NIR-RIT before requiring emergency care for coronavirus disease 2019 (COVID-19). The newly discovered variants underwent enzymatic, thermostability, and structural analyses to assess their impact on the endoproteolytic activity of M^{pro} variants and their sensitivity to NIR [25]. To our knowledge, this is the first multi-institutional study to report on clinical, biochemical, and structural aspects of low-frequency antiviral resistance mutations in SARS-CoV-2 after NIR-RIT exposure. Our findings reveal a unique evolutionary pathway for viral resistance, including mutations outside the M^{pro} active site and cross-resistance to different M^{pro} inhibitors, NIR and C5a [25].

METHODS

Study Design and Samples
Medical records from 2 hospital systems were screened to identify patients with SARS-CoV-2 infections, confirmed by reverse transcription polymerase chain reaction (RT-PCR) between February 2022 and July 2023. A total of 1528 patients tested positive for SARS-CoV-2 via RT-PCR. Among these patients, 17 had previously received a course of NIR-RIT and returned to the hospital still testing positive for SARS-CoV-2. The study was approved by the research ethics boards of the 2 hospitals (REB No. 05-0116-C and 04-0083).

Whole-Genome Sequencing
Nasopharyngeal swabs from patients with SARS-CoV-2 underwent whole-genome sequencing as has been previously described. Briefly, sequencing libraries were created from overlapping amplicons using 2 primer pools. NIR-RIT–treated samples used ARTIC version 4.1 primers, while untreated controls were sequenced with varying primer schemes based on collection dates: (1) ARTIC version 4 for February to March 2022, (2) ARTIC version 4.1 for March to October 2022 [26], and (3) Midnight version 3 for October 2022 to July 2023 [27]. Libraries were prepared with unique barcodes and pooled for sequencing. Samples from treated patients were sequenced along with a PhiX control on a MiniSeq platform (Illumina) while samples from untreated patients were sequenced on GridION instruments (Oxford Nanopore Technologies). Analyses of samples from treated patients were performed using a validated analytical workflow (SIGNAL) [28], while the untreated samples were analyzed using the ARTIC field bioinformatics pipeline [29]. Output from these pipelines was processed using a nationally standardized quality control workflow (ncov-tools) [30]. Low-frequency variants were called using freebayes (version 1.3.8) from the primer-trimmed reads aligned to accession MN908947.3, requiring a minimum coverage of 10, a minimum variant fraction of 0.10, and a minimum variant quality of 50 [31].

M^{pro} in Cellulo Endoproteolytic Activity
Caco-2 cells were seeded at 10 000 cells/well in 96-well plates the day before transduction. Cells were transduced with 2 BacMam baculovirus vectors (Molecular Montana), 1 expressing the recombinant SARS-CoV-2 M^{pro} enzyme and the other expressing a green fluorescent biosensor for M^{pro} enzyme activity. After 3 hours, the cells were treated with the compounds and incubated for 25 hours, followed by fixation of the cells with 3.7% formalin for 30 minutes. The cells were washed with phosphate-buffered saline (PBS), and the nuclei were stained with Hoechst 33342 at 1.5 μg/mL for 30 minutes at room temperature. After washing with PBS, the plates were kept in the dark at 4°C until imaging was performed on a high-content screening (HCS) platform (CellInsight CX7 HCS, Thermo Fisher Scientific) with a 10 × objective. The change in the fluorescence biosensor measured the enzyme activity. The endoproteolytic activity with single-compound concentration experiments were repeated 6 times with 2 technical replicates in each experiment. The effect of compounds for each mutation was normalized against the positive control (0.1% dimethyl sulfoxide [DMSO]).

Half-Maximal Inhibitory Concentration Curves
Half-maximal inhibitory concentration (IC$_{50}$) experiments were repeated 3 times for each compound, with 2 technical replicates in each experiment. Intracellular fluorescence was determined by treating the Caco-2 cells transduced with 2 BacMam

baculovirus vectors for 25 hours with serially diluted compounds. Fluorescence levels were interpolated to negative control (0.1% DMSO, no protease) = 0, and positive control (0.1% DMSO, protease) = 100. The GraphPad Prism 10 nonlinear regression fit modelling variable slope was used to generate a dose-response curve ($Y = Bottom + [Top-Bottom]/[1 + 10^{\wedge}(LogIC_{50}-X)*HillSlope]$), constrained to top = 100, bottom = 0.

Expression and Purification of M^{pro} Mutants

The full-length SARS-CoV2- M^{pro} (UniProt P0DTD1) was cloned into a modified pet28a plasmid with an N-terminal dual His-SUMO tag [32]. The P132H, P132H/L58F, and P132H/L67V/K90R mutants of M^{pro} were generated using QuickChange Site-Directed Mutagenesis kit (Agilent Technologies) and verified by sequencing. Protein expression occurred as per literature standards [7, 32] in *Escherichia coli* BL21 (DE3) at 37°C in Luria-Bertani media with kanamycin, induced at an optical density at 600 nm of approximately 1.0 by adding isopropyl B-D-1-thiogalactopyranoside (IPTG) to 1 mM, then cooled to 16°C. Cells were harvested 5 hours postinduction.

Cell pellets were resuspended in lysis buffer (Sigma Aldrich) and lysed via sonication. This was centrifuged, and the supernatant was loaded onto a gravity flow column with HisPur nickel-Nitrilotriacetic acid (Ni-NTA) resin (Thermo Fisher) equilibrated with a purification buffer. The column was washed with 50 mM imidazole and eluted with 300 mM imidazole. Fractions with M^{pro} were pooled, concentrated, and buffer-exchanged using an Amicon Ultra filter. The sample was concentrated to approximately 10 mL and incubated with SUMO protease at 4°C overnight to cleave the His-SUMO tag. Unwanted proteins were removed using Ni-NTA resin, collecting the cleaved M^{pro} flow through. This sample was concentrated to 1 mL and purified by gel-filtration chromatography with a Superdex 200 Increase column. Fractions containing M^{pro} were pooled, concentrated to > 10 mg/mL, and flash-frozen in liquid nitrogen for storage at −80°C.

Crystallization, Data Processing, and Analysis of M^{pro} P132H Alone and in Complex With M^{pro} Inhibitor C5a

Crystals of the P132H mutant were obtained via sitting drop vapor diffusion, using 0.8 µL of M^{pro} P132H and 0.8 µL of a reservoir solution (40 µL) containing 0.1 M Tris pH 8, 15% PEG 8000, and 10% ethylene glycol. Apoenzyme crystals were crushed with a Seed Bead kit to create seed stock for generating inhibitor cocrystals. For these, C5a [21] was added to a final concentration of 0.7 mM and 1% DMSO. Sitting drops were streak-seeded with apoenzyme, and crystals were soaked in cryoprotectant before freezing.

Diffraction data were collected at the CMCF-BM beamline at the Canadian Light Source using a Pilatus3 S 6M detector. Data processing involved xia2 and XDS, with reduction via Aimless [33] and correction for anisotropic diffraction using the STARANISO server. Phasing was performed by molecular replacement using Phaser with Protein Data Bank (PDB) 7JOY chain B as the model, followed by model building and refinement using Coot and Phenix refine [34]. Model validation was conducted with MolProbity. Analyses of C5a- M^{pro} interaction were carried out using PyMOL (PyMOL Molecular Graphics System, version 2.1, Schrödinger, LLC) and ChimeraX [35]. AlphaFold3 [36] was used to assess the structural mutant combinations P132H, L58F/P132H, and L67V/K90R/P132H in the context of the M^{pro} dimer.

Assessing Thermal Stability of M^{pro} Variants by Differential Static Light Scattering

The thermal stability of M^{pro} variants was studied by differential static light scattering using the StarGazer-2 system (Harbinger Biotechnology). Samples were prepared to a final concentration of 1 mg/mL in the presence or absence of 60 µM NIR for each M^{pro} variant, and 10 µL of each protein was loaded in triplicate into a clear-bottom plate (Corning) at 1 mg/mL and wells were covered with 10 µL of mineral oil. The plate was heated from 25°C to 85°C at 1°C/min and images were taken every 0.5°C. Pixel intensities in each well were integrated using the Stargazer AIR software and intensities were plotted against temperature to yield T$_{agg}$ values for each sample [37].

RESULTS

Cohort Description

Among the 1528 patients screened with emergency department visits or hospitalizations for COVID-19, 17 (1.1%) had received

Table 1. Characteristics of the Patients With Detectable SARS-CoV-2 After Therapy With NIR-RIT

Patient Characteristics	Value
Median age, y, n (range)	82 (69–96)
Female sex, n (%)	10 (59)
Comorbidities, n	
At least 1	16
Lung disease	7
Dementia	4
Cerebrovascular or other neurologic disease	7
Active cancer	4
Cardiac disease	4
Diabetes mellitus	2
Other immunocompromising condition	1
Receipt of NIR-RIT before ED visit/hospitalization, n	17
Patients still receiving NIR-RIT at admission, n (%)	6 (35)
Days of NIR-RIT received before NP swab, median (range)	3 (3–14)
Patients not receiving NIR-RIT at admission, n (%)[a]	11 (65)
Days from end NIR-RIT to admission, median (range)	6 (1–37)

Abbreviations: ED, emergency department; NIR-RIT, nirmatrelvir-ritonavir; NP, nasopharyngeal.
[a]Of these, 9 had completed a 5-day course of therapy before their NP swab, and 2 had discontinued NIR-RIT after 1 and 4 days.

Table 2. Low-Frequency Variants in M^pro Identified in NIR-RIT–Treated Patients

| Patient | Immunocompromised | NIR-RIT Therapy | | Mutation |
		Days of Therapy Before NP Swab	Days From End of Therapy to Admission	
PAX03	Yes	5	8	D48D, L58L, P132H
PAX04	No	5	6	a
PAX06	No	5	1	D48D, P132H
PAX11	Yes	5	37	P132H
PAX14	No	5	2	D48D, L58F, P132H
PAX15	No	5	28	F8F, D48D, P132H
PAX16	No	4	10	P132H
PAX19	No	5	6	a
PAX31	Yes	5	6	D48D, P132H
PAX33	No	5	10	a
PAX35	No	3	…	D48D, L67V, K90R, P132H
PAX36	No	3	…	D48D, P132H
PAX41	No	4	…	D48D, L67V, K90R, P132H
PAX42	Yes	3	…	D48D, P132H
PAX43	No	2	1	D48D, P132H
PAX45	No	3	…	D48D, P132H
PAX46	No	2	…	D48D, P132H

Abbreviations: NIR-RIT, nirmatrelvir-ritonavir; NP, nasopharyngeal.
[a]Unable to generate sequence data.

NIR-RIT treatment before presentation, and all were hospitalized. The median age of patients was 82 years (range, 69–96 years), with 59% (n = 10) being female (Table 1). Of these, 6 (35%) patients required hospitalization before completing their 5-day course of NIR-RIT, and 11 (65%) had completed a 5-day course before admission (Table 1 and Table 2). Patients had a median of 2 comorbidities (range, 0–5), with 1 patient having no underlying comorbidities. Lung and neurologic conditions were the most common (Table 1; specific comorbidities found in Supplementary Table 1).

### Identification of Novel Low-Frequency Mutations

A total of 91 samples were sequenced, including 74 from patients who did not receive NIR-RIT before admission (Figure 1). Sequencing revealed that mutations D48D (C > T) and P132H were present in 88% of patients, including those in the control group. These mutations are prevalent (> 95%) in the Omicron variant B.1.617.2, which was the predominant strain during the sample collection period [38]. In the control group, 53% of the detected variants were synonymous.

Four mutations—D48D, L67V, K90R, and P132H—were observed individually in both groups. However, the L67V and K90R mutations were exclusively observed together in the NIR-RIT–treated group, a pattern not seen in the control group (Supplementary Figure 1). Notably, the 2 patients who exhibited L67V and K90R, along with D48D and P132H, were from Hospital B and linked to an outbreak. Additionally, 2 novel variants were identified at position L58: L58F and a nonsynonymous mutation, L58L (C > U). Sequencing did
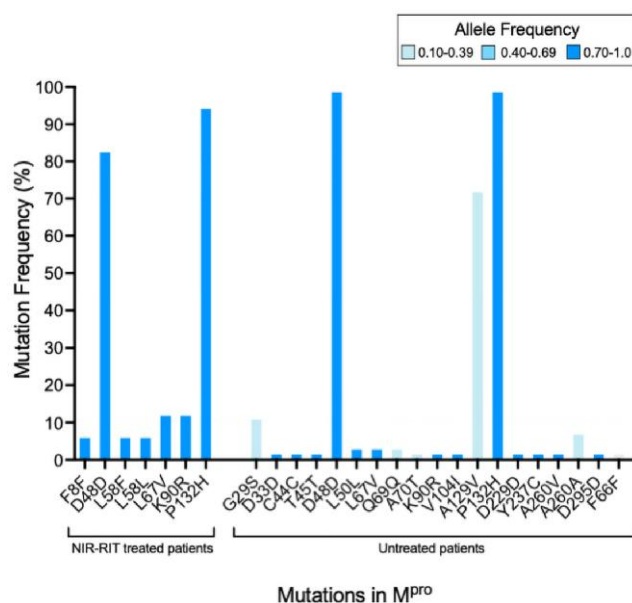
Figure 1. Low-frequency variants in the main viral protease. Low-frequency mutations were identified by whole-genome sequencing in the M^pro found in all patients. Allele frequency within a patient is indicated by color. Frequency of the mutation within the population is shown on the y-axis. Abbreviations: M^pro, main protease; NIR-RIT, nirmatrelvir-ritonavir.

not reveal any previously described resistance mutations in the consensus sequence of the viral protease, and none of the patients exhibited low-frequency variants typically associated with NIR-RIT resistance, such as L50F and E166A/V (Figure 1 and Table 2).
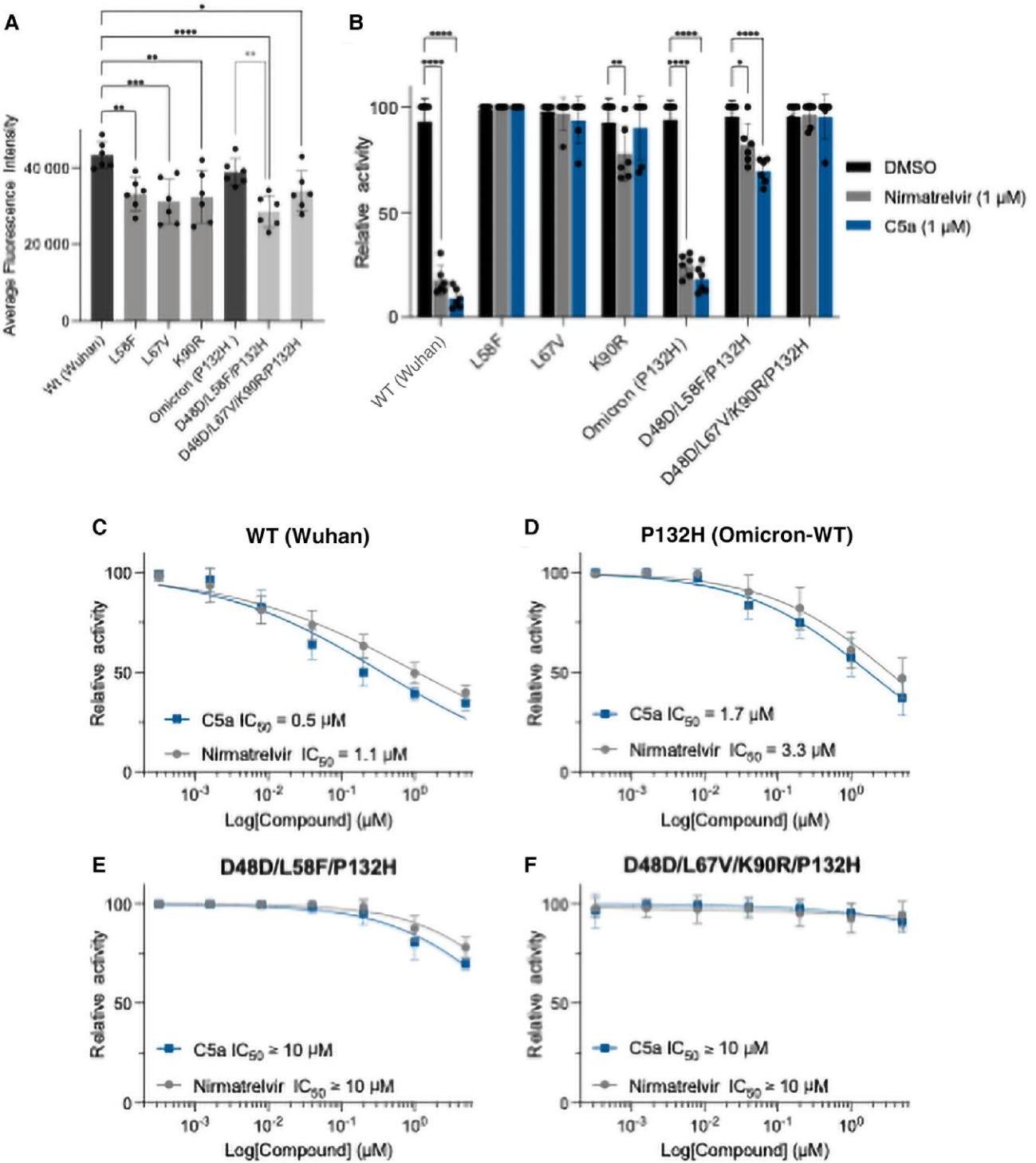
Figure 2. Impact of novel mutations in M^pro endoproteolytic activity of SARS-CoV-2 in cellulo. Cells were transduced with vectors to express the recombinant SARS-CoV-2 M^pro WT or mutants and 3CLglow biosensor, $n = 6$ (A), following treatment with single concentration, $n = 6$ (B) or serial dilution concentrations of nirmatrelvir (grey circles) or C5a (blue squares) (C–F). Nonlinear regression was used for IC_{50} curve fitting. Data are expressed as mean ($n = 3$), with significance determined by 1-way ANOVA. *$P < .05$, **$P < .01$, ***$P < .001$, ****$P < .0001$. Error bars are standard deviation. Abbreviations: DMSO, dimethyl sulfoxide; IC_{50}, half-maximal inhibitory concentration; M^pro, main protease; WT, wild type.

Effects of the Newly Identified Mutations on M^{pro} Endoproteolytic Activity and Inhibitory Profile in Human Cells

We used a green fluorescent biosensor to evaluate the effects of specific low-frequency variants [25]. The M^{pro} variants expressed in Caco-2 cells by transduction included D48D/L58F/P132H, D48D/L67V/K90R/P132H, L58F, L67V, K90R, and P132H. For M^{pro} activity, the cells were also transduced with a vector encoding a green fluorescent biosensor. Our results demonstrated that almost all M^{pro} variants show between 20% and 30% reduction in their activity compared to the wild-type (WT) M^{pro} corresponding to the ancestral (Wuhan) SARS-CoV-2 sequence (Figure 2A), while the activity of mutation P132H, prevalent in the Omicron lineage, was unaffected. The only mutant showing a difference in their activity against M^{pro} Omicron was D48D/L58F/P132H (Figure 2A). However, when we compared the activity of the mutant M^{pro} variants identified in this study with previously reported mutations associated with NIR resistance in vitro, such as L50F/E166A/L167F [11–13] or naturally occurring H172Y, Q189E or Q192T [39], we found that the endoproteolytic activity was affected, with a 60%–80% reduction (Supplementary Figure 2A).

We evaluated the effects of the protease inhibitors NIR and C5a on the activity of the M^{pro} variants. C5a is a noncovalent, catalytic-site-directed M^{pro} inhibitor [25]. We repeated the M^{pro} bioassay described above, incorporating the inhibitors into the experimental setup. We confirmed that NIR and C5a effectively inhibit the activity of both M^{pro} WT and P132H (Omicron) (Figure 2B–D). Testing the mutants L58F and L67V on the WT background showed higher levels of resistance to NIR and C5a compared to K90R NIR resistance (Figure 2B). However, when combining mutations with P132H, resistance to the inhibitors was minimal. This contrasts with the double and triple mutants L50F/E166A/L167F, which showed reduced resistance with slight differences in inhibition between NIR and C5a (Supplementary Figure 3B). D48D/L58F/P132H (variant 1) presented > 10-fold increases in IC$_{50}$ to NIR and C5a, respectively (Figure 2E). The D48D/L67V/K90R/P132H (variant 2) mutant displayed near-complete resistance (Figure 2F). While minimally affecting enzymatic activity, they significantly increased inhibitor resistance, warranting further structural analysis of the M^{pro} variants.

Structure of M^{pro} P132H in Complex With C5a and Analysis of the Structural Impact of Clinical Mutants

To explore the impact of the clinical mutants, we determined structures of the P132H mutant alone and in complex with C5a (Supplementary Tables 2 and 3). These were then used as templates to analyze the identified mutants.

P132 is remote from the substrate binding site, approximately 22 Å to nucleophilic cysteine C145, and the structure of the P132H mutant is similar to WT (Wuhan) [40] (Figure 3A). This is consistent with the similar enzymatic activity and inhibition observed here (Figure 2A) and by others [41]. P132 resides

within the loop that connects β-strands 10 (residues 121–130) and 11 (147–153), proximal to C145. The P132 prolyl side chain faces the loop that links the catalytic and dimerization domains (within 4 Å of residues D197, T198, I200, and E240; Supplementary Figure 4A). Other residues within 4 Å of P132 reside within the catalytic domain (M130, R131, N133, F134, and P108), but are still relatively far from the active site (Supplementary Figure 4). The presence of the inhibitor in structures P132H + C5a and WT + C5a [25] results in D197 being within 4 Å of residue 132. This brings D197 close to R131, allowing it to form an electrostatic interaction. Different rotamers of P132H suggest it does not play a critical role in interacting with D197. A similar level of contact surface between P132H or P132 and D197 suggests polarity differences are not significant. Because the added interaction with D197 occurs with and without the P132H mutation it is unlikely this reveals a mechanism for resistance. The complex of P132H with C5a (Figure 3B,C) shows the inhibitor adopts the same pose in the active site as we previously observed for WT M^{pro} [24], consistent with the ability of C5a to inhibit P132H to the same level as WT (Figure 2B–D). Similarly, P132H does not appreciably affect the structure of the substrate binding site extending away from the active site.

We mapped the positions of the clinical mutants onto the P132H M^{pro} structure (Figure 3A). Although none are located in the active site or substrate binding site, they cluster in the N-terminal domain and form second and third shell interactions with the substrate binding site. Notably, L58F interacts with I43, a key area containing residues critical for catalysis (H41) and substrate binding (M49, which shows significant dynamism across different substrates or inhibitor complexes [32]). Furthermore, L67V contacts T21 on β-strand 1, which forms part of the substrate S3′ pocket. To explore this, we generated models of L58F/P132H and L67V/K90R/P132H (Figure 3D). Although the structures are conserved, in both cases the region covering residues 45–54 is perturbed compared to P132H alone (arrow in Figure 3D), supporting the potential disruption of this domain. When probed with differential static light scattering, we found that the thermal stability of the mutants is decreased relative to WT. Furthermore, while WT M^{pro} has ΔT$_{agg}$ of +8°C upon NIR binding, this is reduced to 5°C when all sites are mutated (Supplementary Figure 3). Thus, like the P132H mutant alone [41], the mutants here impair M^{pro} stability without affecting activity (Figure 2). However, unlike P132H, which exhibits WT levels of inhibition, the activity of the mutants, especially variant 2, is less affected by NIR and C5a (Figure 2) with a corresponding weakened thermal stabilization on binding (Supplementary Figure 3). The exact cause of this decrease in inhibitor efficacy is unclear; however, the results suggest protein destabilization that indirectly impacts inhibitor binding without affecting activity. Further experiments are required to test this hypothesis.
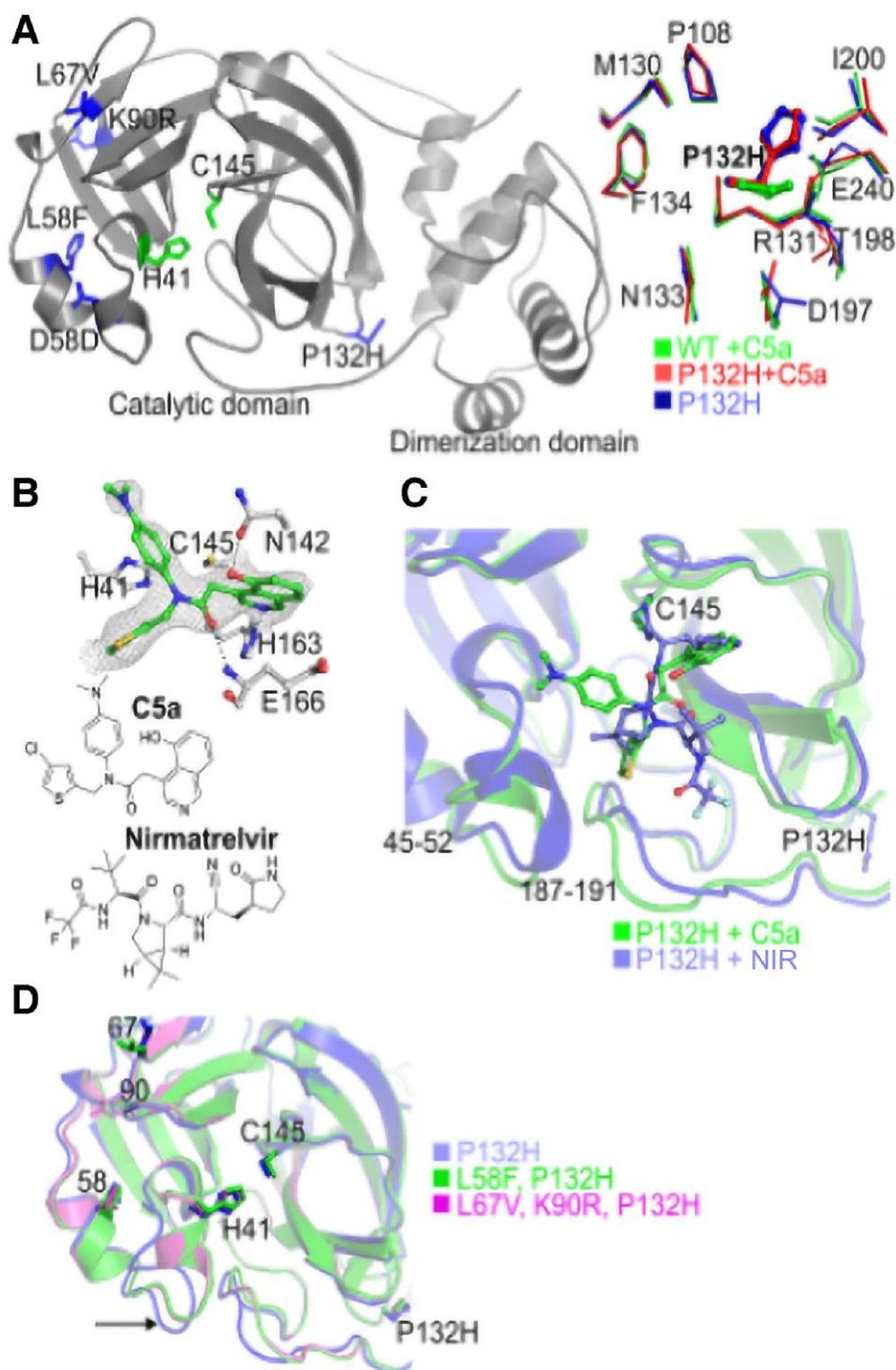
Figure 3. Structure-based analysis of SARS-CoV-2 M^pro mutant. *A*, Localization of mutants mapped onto the M^pro P132H structure shown in ribbon superposed on a surface rendering. Mutant positions are colored blue and labeled. Catalytic residues H41 general base and C145 nucleophile are shown in green. On the right is a superposition of the M^pro region localized to the P132H mutant in our apoenzyme (blue) and C5a bound structures (red) determined here, as well as a prior structure of the WT M^pro with C5a in green (PDB: 8SXR). *B*, 2Fo-Fc refined electron density in grey mesh contoured at 1 sigma. C5a forms hydrogen bonds (black dashes) to residues Asn142, His 163, and Glu 166 (carbon grey, nitrogen blue, sulfur yellow). The catalytic residues C145 and H41 are shown for reference. Chemical structures of C5a and nirmatrelvir are shown below. *C*, Superposition of the P132H M^pro structure with C5a determined here (green protein ribbon and ball and stick C5a) and with that determined previously with nirmatrelvir (blue protein ribbon and ball and stick inhibitor; PDB: 7TLL). *D*, Comparison of AlphaFold 3 structural predictions of L58F/P132H (green) and L67V/K90R/P132H (magenta) mutants identified in this study. Black arrow indicates region (residues 45–54) of greatest difference between these forms. Abbreviations: M^pro, main protease; NIR, nirmatrelvir; PDB, Protein Data Bank; WT, wild type.

DISCUSSION

Our study furthers our understanding of resistance to NIR-RIT by identifying novel mutations and characterizing their potential mechanisms of resistance. The mutations reflect complex adaptive strategies that affect protein stability and inhibitor susceptibility. These mutations, although not targeting the active sites of the M^{pro} protein, influence residues important for enzyme interactions and substrate binding. Several of the mutations identified in this study were previously unreported. The combination of D48D/L67V/K90R/P132H has not been documented [16, 41–44], despite the prevalence of D48D (C > U) and P132H [38], and K90R in Omicron and Beta variants, respectively [38]. Unlike the mutations L50F and E166A/V, which are associated with high resistance levels, these do not directly affect the substrate binding site of M^{pro}. Instead, they form secondary interactions with residues around the substrate binding site or could influence regions involved in enzyme interactions. This suggests a more intricate adaptive mechanism, with mutations like K90R compensating for fitness deficits caused by mutations like L67V, potentially enhancing viral stability and flexibility [13]. Furthermore, P132H reduces M^{pro} thermal stability [41], potentially increasing protein flexibility and altering the enzyme's substrate profile or ligand binding.

In silico modeling supports these findings. For example, superposition of the AlphaFold3 L58F/P132H model and the WT crystal structure (PDB: 7JP1) shows that L58F makes additional contacts with atoms within residues H80, S81, and L87. Superposition of the AlphaFold3 L67V/K90R/P132H model and the WT crystal structure shows that L67V enables an added contact with Q74. These changes could propagate through M^{pro}'s structure and its interaction with NIR-RIT, contributing to biochemical resistance.

Studies have described 2 types of mechanisms for NIR resistance: (1) substitutions that directly affect the substrate binding pocket, resulting in the loss of enzymatic activity with reduced viral fitness; and (2) substitutions that are not directly involved in the substrate binding pocket and are not directly responsible for decreased enzymatic activity [11]. The L58F, L67V, or K90R mutations correspond to the second type of mechanism. These mutations could alter protein structure and dynamics, reducing inhibitor susceptibility while maintaining viral fitness. Indeed, molecular dynamics and machine learning approaches have been used to characterize the drug resistance pathways of M^{pro} mutants [45]. These highlight a complex landscape of mutant phenotypes that impact substrate/inhibitor binding, protein stability, and activity. This is evident in ternary mutant systems where the coevolution of multiple mutations can be mutually compensatory, for example, increasing catalytic activity to account for decreased substrate/inhibitor binding. This aligns with our observation that variant 2 retains similar proteolytic activity to Omicron M^{pro} but exhibits complete resistance to NIR-RIT and C5a, with impacts on protein stability. In contrast, variant 1 shows reduced catalytic activity and partial resistance to inhibitors, while maintaining thermal stability. N-terminal mutations, located far from the catalytic site, are responsible for reducing the protein stability and impacting substrate binding or dimerization, but there are other mutations [6–11, 14] outside the N-terminal domain that can affect the protease activity and are still susceptible to the inhibitors. These findings suggest that while the mutations may not directly interfere with the substrate binding pocket, their impact on protein stability and enzyme dynamics could still confer resistance. This aligns with prior work, highlighting how both active site and distal M^{pro} mutations can reduce NIR binding through altered structural dynamics [45].

We also identified synonymous mutations that may act as springboard mutations. For example, mutations at D48 can destabilize an α-helix above the substrate binding site, impacting inhibitor binding and potentially increasing resistance to NIR-RIT [46]. Most synonymous mutations observed here are C to U, suggesting APOBEC editing of viral RNA, consistent with findings that about 40% of all SARS-CoV-2 nucleotide variations are C to U [47, 48]. These may enhance viral fitness and may make resistance mutations arising from transitions more likely than those from transversions [49].

The study has limitations, including the lack of serial samples to evaluate low-frequency persistence and viral fitness. Additionally, the inability to conduct cell culture studies precludes an assessment of patient infectiousness. The potential underreporting of NIR-RIT use and overlapping hospital catchment areas are also limitations. However, the low percentage of identified patients from multiple institutions is encouraging as this suggests antiviral resistance is infrequent and the barrier to resistance is likely high.

Our study highlights the need for ongoing surveillance for antiviral resistance in SARS-CoV-2. Moreover, although structural changes from mutations may affect drug binding and protease activity, the clinical implications of these mutations require further investigation.

Supplementary Data

Supplementary materials are available at *The Journal of Infectious Diseases* online (http://jid.oxfordjournals.org/). Supplementary materials consist of data provided by the author that are published to benefit the reader. The posted materials are not copyedited. The contents of all supplementary data are the sole responsibility of the authors. Questions or messages regarding errors should be addressed to the author.

Notes

Author contributions. F. J., A. M., and R. A. K. contributed conceptualization. Z. Z., L. F., A. M., L. S., I. M., M. F., and A. L. X. performed methodology, investigations, patient sample collection, and chart review. N. M. D. and P. A. performed

References

1. Hammond J, Leister-Tebbe H, Gardner A, et al. Oral nirmatrelvir for high-risk, nonhospitalized adults with COVID-19. N Engl J Med 2022; 386:1397–408.

2. Owen DR, Allerton CMN, Anderson AS, et al. An oral SARS-CoV-2 M^{pro} inhibitor clinical candidate for the treatment of COVID-19. Science 2021; 374:1586–93.

3. Arbel R, Wolff Sagy Y, Hoshen M, et al. Nirmatrelvir use and severe COVID-19 outcomes during the Omicron surge. N Engl J Med 2022; 387:790–8.

4. Lewnard JA, McLaughlin JM, Malden D, et al. Effectiveness of nirmatrelvir–ritonavir in preventing hospital admissions and deaths in people with COVID-19: a cohort study in a large US health-care system. Lancet Infect Dis 2023; 23:806–15.

5. Mody V, Ho J, Wills S, et al. Identification of 3-chymotrypsin like protease (3CLPro) inhibitors as potential anti-SARS-CoV-2 agents. Commun Biol 2021; 4:1–10.

6. Xie Y, Choi T, Al-Aly Z. Association of treatment with nirmatrelvir and the risk of post-COVID-19 condition. JAMA Intern Med 2023; 183:554–64.

7. Jin Z, Du X, Xu Y, et al. Structure of M^{pro} from SARS-CoV-2 and discovery of its inhibitors. Nature 2020; 582:289–93.

8. Kneller DW, Phillips G, O'Neill HM, et al. Structural plasticity of SARS-CoV-2 3CL M^{pro} active site cavity revealed by room temperature X-ray crystallography. Nat Commun 2020; 11: 3202.

9. Zhang L, Lin D, Sun X, et al. Crystal structure of SARS-CoV-2 main protease provides a basis for design of improved α-ketoamide inhibitors. Science 2020; 368:409–12.

10. Zhu Y, Yurgelonis I, Noell S, et al. In vitro selection and analysis of SARS-CoV-2 nirmatrelvir resistance mutations contributing to clinical virus resistance surveillance. Sci Adv 2024; 10:eadl4013.

11. Duan Y, Zhou H, Liu X, et al. Molecular mechanisms of SARS-CoV-2 resistance to nirmatrelvir. Nature 2023; 622:376–82.

12. Jochmans D, Liu C, Donckers K, et al. The substitutions L50F, E166A, and L167F in SARS-CoV-2 3CLpro are selected by a protease inhibitor in vitro and confer resistance to nirmatrelvir. mBio 2023; 14:e0281522.

13. Iketani S, Mohri H, Culbertson B, et al. Multiple pathways for SARS-CoV-2 resistance to nirmatrelvir. Nature 2023; 613:558–64.

14. Zhou Y, Gammeltoft KA, Ryberg LA, et al. Nirmatrelvir-resistant SARS-CoV-2 variants with high fitness in an infectious cell culture system. Sci Adv 2022; 8:eadd7197.

15. Rosa RB, Dantas WM, do Nascimento JCF, da Silva MV, de Oliveira RN, Pena LJ. In vitro and in vivo models for studying SARS-CoV-2, the etiological agent responsible for COVID-19 pandemic. Viruses 2021; 13:379.

16. Garcia-Segura P, Llop-Peiró A, Novau-Ferré N, et al. SARS-CoV-2 main protease (M-pro) mutational profiling: an insight into mutation coldspots. Comput Biol Med 2025; 184:109344.

17. Sjaarda CP, Lau L, Simpson JT, et al. Prevalence of low-frequency, antiviral resistance variants in SARS-CoV-2 isolates in Ontario, Canada, 2020-2023. JAMA Netw Open 2023; 6:e2324963.

18. Hirotsu Y, Kobayashi H, Kakizaki Y, et al. Multidrug-resistant mutations to antiviral and antibody therapy in an immunocompromised patient infected with SARS-CoV-2. Med 2023; 4:813–24.e4.

19. Zuckerman NS, Bucris E, Keidar-Friedman D, Amsalem M, Brosh-Nissimov T. Nirmatrelvir resistance-de novo E166V/L50V mutations in an immunocompromised patient treated with prolonged nirmatrelvir/ritonavir monotherapy leading to clinical and virological treatment failure—a case report. Clin Infect Dis 2024; 78:352–5.

20. Lee JT, Yang Q, Gribenko A, et al. Genetic surveillance of SARS-CoV-2 M^{pro} reveals high sequence and structural conservation prior to the introduction of protease inhibitor paxlovid. mBio 2022; 13:e0086922.

21. Hermankova M, Ray SC, Ruff C, et al. HIV-1 drug resistance profiles in children and adults with viral load of <50 copies/ml receiving combination therapy. JAMA 2001; 286:196–207.

22. Lima VD, Gill VS, Yip B, Hogg RS, Montaner JSG, Harrigan PR. Increased resilience to the development of drug resistance with modern boosted protease inhibitor-based highly active antiretroviral therapy. J Infect Dis 2008; 198:51–8.

23. Ji H, Kozak RA, Biondi MJ, et al. Next generation sequencing of the hepatitis C virus NS5B gene reveals potential novel S282 drug resistance mutations. Virology 2015; 477:1–9.

24. Wyles D, Dvory-Sobol H, Svarovskaia ES, et al. Post-treatment resistance analysis of hepatitis C virus from phase II and III clinical trials of ledipasvir/sofosbuvir. J Hepatol 2017; 66:703–10.

25. Pérez-Vargas J, Worrall LJ, Olmstead AD, et al. A novel class of broad-spectrum active-site-directed 3C-like protease inhibitors with nanomolar antiviral activity against highly immune-evasive SARS-CoV-2 Omicron subvariants. Emerg Microbes Infect 2023; 12:2246594.

26. ARTIC Network. SARS-CoV-2 V4.1 update for Omicron variant, 2021. https://community.artic.network/t/sars-cov-2-v4-1-update-for-omicron-variant/342. Accessed 31 March 2025.

27. Freed N, Silander O. nCoV-2019 sequencing protocol (RAPID barcoding, 1200bp amplicon). https://www.protocols.io/view/ncov-2019-sequencing-protocol-rapid-barcoding-1200-rm7vz8q64vx1/v3. Accessed 31 March 2025.

28. Nasir JA, Kozak RA, Aftanas P, et al. A comparison of whole genome sequencing of SARS-CoV-2 using amplicon-based sequencing, random hexamers, and bait capture. Viruses 2020; 12:895.

29. Artic-network/fieldbioinformatics. The ARTIC field bioinformatics pipeline. https://github.com/artic-network/fieldbioinformatics. Accessed 14 May 2025.

30. Simpson J. jts/ncov-tools, 2025. https://github.com/jts/ncov-tools. Accessed 31 March 2025.

31. Garrison E, Marth G. Haplotype-based variant detection from short-read sequencing. arXiv, doi: 10.48550/arXiv.1207.3907, 17 July 2012, preprint: not peer reviewed.

32. Lee J, Kenward C, Worrall LJ, et al. X-ray crystallographic characterization of the SARS-CoV-2 main protease polyprotein cleavage sites essential for viral processing and maturation. Nat Commun 2022; 13:5196.

33. Agirre J, Atanasova M, Bagdonas H, et al. The CCP4 suite: integrative software for macromolecular crystallography. Acta Cryst D 2023; 79:449–61.

34. Afonine PV, Poon BK, Read RJ, et al. Real-space refinement in PHENIX for cryo-EM and crystallography. Acta Cryst D 2018; 74:531–44.

35. Pettersen EF, Goddard TD, Huang CC, et al. UCSF chimeraX: structure visualization for researchers, educators, and developers. Protein Sci 2021; 30:70–82.

36. Abramson J, Adler J, Dunger J, et al. Accurate structure prediction of biomolecular interactions with AlphaFold 3. Nature 2024; 630:493–500.

37. Senisterra GA, Markin E, Yamazaki K, Hui R, Vedadi M, Awrey DE. Screening for ligands using a generic and high-throughput light-scattering-based assay. J Biomol Screen 2006; 11:940–8.

38. Ullrich S, Ekanayake KB, Otting G, Nitsche C. Main protease mutants of SARS-CoV-2 variants remain susceptible to nirmatrelvir. Bioorg Med Chem Lett 2022; 62:128629.

39. Hu Y, Lewandowski EM, Tan H, et al. Naturally occurring mutations of SARS-CoV-2 main protease confer drug resistance to nirmatrelvir. ACS Cent Sci 2023; 9:1658–69.

40. Lee J, Worrall LJ, Vuckovic M, et al. Crystallographic structure of wild-type SARS-CoV-2 main protease acyl-enzyme intermediate with physiological C-terminal autoprocessing site. Nat Commun 2020; 11:5877.

41. Sacco MD, Hu Y, Gongora MV, et al. The P132H mutation in the main protease of Omicron SARS-CoV-2 decreases thermal stability without compromising catalysis or small-molecule drug inhibition. Cell Res 2022; 32:498–500.

42. Bloom JD, Beichman AC, Neher RA, Harris K. Evolution of the SARS-CoV-2 mutational spectrum. Mol Biol Evol 2023; 40:msad085.

43. Almalki SSR, Izhari MA, Alyahyawi HE, et al. Mutational analysis of circulating Omicron SARS-CoV-2 lineages in the Al-Baha region of Saudi Arabia. J Multidiscip Healthc 2023; 16:2117–36.

44. Yashvardhini N, Kumar A, Jha DK. Analysis of SARS-CoV-2 mutations in the main viral protease (NSP5) and its implications on the vaccine designing strategies. Vacunas (English edn) 2022; 23:S1–13.

45. Wang J, Xie J, Yu Y, Ji Y, Dong H, Li Y. Enhancing the understandings on SARS-CoV-2 main protease (M^{pro}) mutants from molecular dynamics and machine learning. Int J Biol Macromol 2025; 310:143076.

46. Moghadasi SA, Heilmann E, Khalil AM, et al. Transmissible SARS-CoV-2 variants with resistance to clinical protease inhibitors. Sci Adv 2023; 9:eade8778.

47. Simmonds P. Rampant C→U hypermutation in the genomes of SARS-CoV-2 and other coronaviruses: causes and consequences for their short- and long-term evolutionary trajectories. mSphere 2020; 5:e00408-20.

48. Matyášek R, Kovařík A. Mutation patterns of human SARS-CoV-2 and bat RaTG13 coronavirus genomes are strongly biased towards C > U transitions: indicating rapid evolution in their hosts. Genes (Basel) 2020; 11:761.

49. Kim K, Calabrese P, Wang S, et al. The roles of APOBEC-mediated RNA editing in SARS-CoV-2 mutations, replication and fitness. Sci Rep 2022; 12:14972.